Independent estimates of carbon stocks in croplands: UAV-LiDAR and machine learning vs. eddy covariance

Jaime C. Revenga[1], Katerina Trepekli[1], Rasmus Jensen[1], Pauline S. Rummel[1], Thomas Friborg[1]

[1]Department of Geosciences and Natural Resources Management (IGN), Copenhagen University, Denmark
[1]Øster Voldgade, 10, 1350 Copenhagen, Denmark

Key Points:

- The plant carbon budget in croplands estimated from UAV-LiDAR and machine learning regression is comparable with the carbon ecosystem uptake estimated via the eddy covariance technique.

- The relative match between the UAV-based method and the flux-based method along the two growing seasons (2.5 ± 10.4 % in 2020, and -9.0 ± 13.3 % in 2021) indicates that the UAV-based method is a valuable tool for plant carbon stock assessments, adaptive crop management practice and nutrient cycling studies in croplands.

- The proposed method has the potential to estimate cumulative CO_2 fluxes over areas not covered by direct eddy covariance flux measurements.

Corresponding author: Jaime C. Revenga, `contact:  jar@ign.ku.dk`

Abstract

Understanding sequestration of organic carbon (C) in agroecosystems is of primary importance for greenhouse gas (GHG) accounting in managed ecosystems, reducing the environmental footprint of land use, and inform crediting programs. However, a broader application of precise C accounting is currently constrained by a limited number of direct flux measurements. Aside well-studied ecosystems via the eddy covariance technique (EC), many still bear significant uncertainty. In this study, we propose and evaluate a method for estimating accumulated C stocks in agricultural sites, by assessing the plant aboveground carbon (AGC) throughout the growing season using mobile platforms and machine learning (ML) regression methods. Then, we benchmark these estimates with CO_2 fluxes derived from the eddy covariance method from the ICOS DK-Vng site in Denmark. We utilized a light detection and ranging (LiDAR) sensor onboard an unstaffed aerial vehicle (UAV) to derive the structural characteristics of crops, and we conducted in parallel destructive field-based measurements of AGC. Then, we designed a ML pipeline to provide estimates of AGC as a supervised regression problem, using the LiDAR-derived point cloud data to extract predictive features and the AGC labels as ground-truth target values. The best performing ML model attained predictions of $R^2 = 0.71$ and $R^2 = 0.93$ at spatial resolutions of 1 m^2 and 2 m^2, respectively. The C content in the aboveground plant components was assessed via laboratory analysis (46.6 $\pm$ 0.3% of C-to-biomass in barley and 47.7 $\pm$ 0.3% in wheat), while the belowground components (root allocation and rhizodeposition) were estimated based on a phenology-dependent allometric ratio. The cumulative value of C uptake along the growing season (i.e. NPP) was compared with the difference of C predictions between every two UAV-LiDAR survey dates, finding an optimal disagreement between methods below $\pm$ 10% in two different cereal crops. Various experimental set-ups are evaluated as well as the sources of uncertainty resulting from the sampling design.

1 = Introduction =

The agricultural sector is the world's second-largest greenhouse gas (GHG) emitter, after the energy sector, accounting for a quarter of total global anthropogenic GHG emissions [1]. While agriculture is a driver of climate change, the observed climate alterations have in turn challenged the global crop productivity in the last decades [2, 3]. In the absence of technological adaptations and dedicated mitigation measures [4], the environmental effects of agriculture could increase by 50–90 % [5], and the global crop productivity might be reduced a 17 % by 2050 [6]. However, in most countries, the accounting of emissions for land-use and agriculture relies on simple upscaling of standardized values, with little to no data-driven validation procedures. To date, the adoption of climate-resilient and low-emission practices in agriculture has not yet reached the recommended levels [5]. This is hindering accurate GHG accounting as well as attaining environmental and economically efficient solutions.

Monitoring carbon (C) sequestration and CO_2 emissions from croplands is a prerequisite for the effective design of sustainable agricultural management schemes. In a changing global climate, different regions undergo contrasting extreme weather events such as drought, heavy precipitation, shifts in timing and length of growing seasons, or heat stress [7]. This highlights the necessity to quantify the C sequestration capacity with techniques tailored to specific ecosystems' conditions. In this context, precision agriculture (PA) is regarded as a promising set of methods for sustainable intensification, in order to close yield gaps while reducing GHG emissions [8, 9, 10]. PA targets the reduction of agriculture's impact on the environment, while optimizing crop yield [11] with data-driven methods.

The standard framework to account for the transit of atmospheric CO_2 is the net ecosystem exchange (NEE) [12], i.e. the net CO_2 flux at the atmosphere-biosphere interface (Figure 1). NEE is calculated as the difference between CO_2 uptake (i.e. gross primary productivity, GPP) and release of CO_2 via respiratory losses (R_{eco}) [..]. Another commonly used metric in ecosystem budgeting is net primary productivity (NPP), which, unlike NEE, does not explicitly include soil-derived fluxes and heterotrophic respiration. Therefore, it reflects the photosynthetic productivity of vegetation alone [13]. Thus, NPP is the most direct surrogate measure for plant growth provided by the flux-based eddy covariance framework.

At the ecosystem scale, C budgets are usually reported as a range of confidence for C estimates, rather than specific values [14]. This is due to the fact that ecosystem-level estimates are bound to co-ocurring complex phenomena, so that it is necessary to count on certain assumptions (e.g. negligible levels of lateral carbon fluxes and heterotrophic respiration, atmospheric turbulence conditions reached, etc.) which affect the estimates' accuracy. In fact, studies focused on different regions have reported large inter-annual variability in C fluxes from croplands, which act either as net sinks [15], net sources [16, 17], or as relatively C neutral [18]. In order to assess the consistency of the net ecosystem carbon balance (NECB), established approaches involve comparing a measured quantity (e.g. NEE) obtained at the same temporal and spatial scale using independent methods [19, 20, 21, 22, 23]. This is usually done via either: (i) micrometeorological methods to assess the ecosystem-atmosphere fluxes; (ii) inventories of stock changes in the biomass and soil; or (iii) bottom-up modelling of ecophysiological processes from flux chamber measurements. Such consistency assessments require that all NECB components are estimated during the same time intervals [24].

In practice, the components of the NECB are directly measured by the eddy covariance (EC) technique or derived from such measurements [25], which is to date the state-of-the-art to obtain ecosystem-level flux estimates. However, there are limitations associated with the EC method, namely, (i) being bound to local measurements with costly instrumentation fixed to the ground, and (ii) requiring specific atmospheric conditions.This method also involves the assumption of representativeness, meaning that areas monitored by the EC method are expected to be representative of broadly defined ecosystem types. However, observational gaps exist [26] and single ecosystem types may not be sufficiently account for the effects of local environmental conditions and management practices. Hence, it is needed to advance methods to improve the flexibility of C estimates, where approaches based on mobile platforms have proven useful [26, 27, 28, 29].

The primary motivation for advancing methods based on Unmanned Aerial Vehicles (UAVs) is to leverage the flexibility and scalability that mobile platforms offer. This allows for independence from restrictions associated with the use of fixed instrumentation. In the last decade, UAV methods developed for crop phenotyping and flux research have provided significant advances [26, 27, 28, 29]. The integration of UAV-based data and ecosystem modelling has seen recent advances: Wang et al. (2020) [26] introduced a method for estimating interpolated land surface fluxes derived from a combination of UAV-based imagery and a dynamic modelling, finding that the UAV-based method proved useful in calibrating soil and vegetation parameters, achieving C flux estimates within 13-15% of agreement with the EC measurements. Moreover, UAV-based remote sensing is increasingly used to assess aboveground biomass (AGB) and carbon stocks, thanks to mobile sensors' capacity to capture land surface variables with high spatial resolution and flexible revisit times [30]. To date, the majority of studies use UAV-photogrammetry (e.g. structure-from-motion techniques) to calculate AGB as a function of plant height metrics (e.g. maize [31, 32, 33], corn [34], rice [35], barley [36, 37] cotton [38] , or winter wheat [39, 40]). Yet another line of research aims to assess AGB as a function of vegetation indices using spectrally resolved sensors (e.g. spring wheat [41], winter wheat [42, 43, 44], corn and soybean [45], and rice [46]).

More recently, the advent of mobile light detection and ranging sensors (LiDAR) has not only upgraded the spatial resolution of data sets, but also included the vertical component, creating truly volumetric representations (i.e. point clouds). This has allowed to enhance crop phenotyping [47] and map AGB in croplands at a sub-meter resolution [30] by leveraging the structural information of vegetation from 3D point clouds. UAV-LiDAR methods have provided a workaround to previous obstacles in UAV-based crop phenotyping, namely the spectral saturation in image-based vegetation indexes, especially during maturity of crops [...].

Here, we explore the level of agreement between two independent methods to estimate cumulative plant C in cereal croplands: (i) UAV-LiDAR surveying combined with ML regressions, and (ii) flux-based EC measurements. We compare simultaneous and independent estimates of photoassimilated C stocks, in a crop field in North Jutland (DK), over two consecutive years. Specifically, we propose and evaluate a method to estimate *in situ* plant C using UAV-LiDAR and machine learning (ML) regressions, and compare the results obtained with the respective NPP during identical time intervals. The motivation of this study is to leverage the capabilities of UAV-LiDAR sensors and a ML regressions in order to provide estimates of plant C stocks in croplands, thereby contributing to advancing current techniques in ecosystem CO_2 budgeting from mobile platforms.
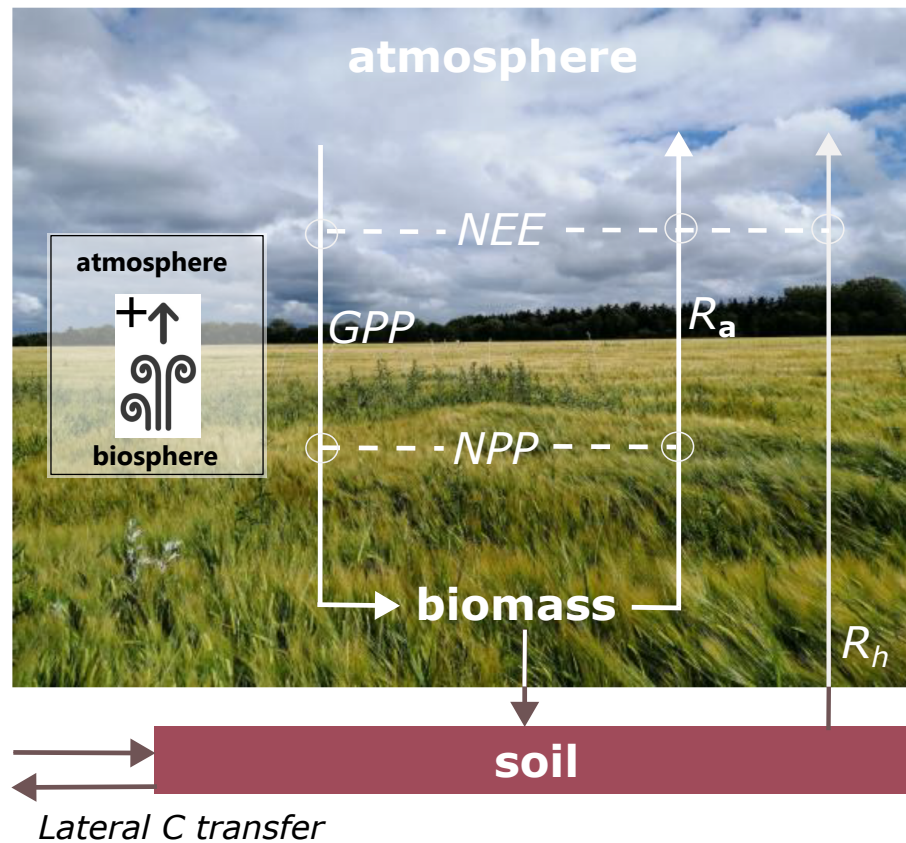
Figure 1. Components of the net ecosystem carbon balance (NECB). The inset on the left indicates the sign convention for fluxes calculation. NEE: net ecosystem excange. GPP: gross primary productivity. NPP: net primary productivity. NEE: net ecosystem exchange. R_a: autotrophic respiration. R_h: heterotrophic soil respiration. Lateral carbon transfer refers to human intervention (e.g. harvest, fertilization).

2 = Materials and Methods =

2.1 Study Area

The study area (Figure 2) is a conventionally managed cropland site located around an Integrated Carbon Observation System (ICOS) [48] class-1 ecosystem station at Voulund, (DK-Vng) in Mid-Jutland, Denmark (56.037476N, 9.160709E). Located on the eastern part of the Skjern River catchment, covering an area of ca. 13 ha. The field is a flat plain at an altitude of 64-68 m above mean sea level, with smooth undulations and a slight slope to the northwest. The ploughing layer (30 cm deep) sits on a sandy soil (>99%) with pebble inclusions of ca. 3-5 diameter. The water-table depth lies at 5.5 ± 1 m below ground. The region presents a humid temperate climate characterized by a mean annual precipitation of 961.0 mm, mean annual temperature of 8.1 ˚C, and usually overcast or scattered cloud cover (mean annual incoming short-wave radiation of 108 W/m^2). For an insightful description of both functional and topographic characeristics of the Voulund agriculural site, the reader is referred to Jensen et al. (2016) [18]

The crops investigated were spring barley (*Hordeum vulgare L.*) and winter wheat (*Triticum aestivum L.*) during 2020 and 2021, respectively. The growing period of the barley crops lasted

Figure 2. Location of the study site (⋆) in Mid-Jutland (DK). The inset shows a top-down view of the field site and the surrounding area. Source: www.icos-cp.eu and Google Earth Engine.

from the end of 04/2020 (seedling emergence) to the end of 08/2020 (harvest), following a similar cycle in the 2021 season. In 2021, the growing period of winter wheat extended from 01/2021 (seedling emergence) until the end of 08/2021 (harvest). The conventional agricultural practice at the site included the application of fertilizers in the form of pig slurry, according to ministerial regulations [49], pesticides and fungicides along the growing season, as well as sufficient irrigation to prevent water stress [18]. This corresponds to a maximum amount of fertilizer of 159 (N) and 21 (P) kg/ha and 202 (N) and 19 (P) kg/ha for spring barley and winter wheat, respectively.

2.2 UAV-LiDAR Survey and Point Cloud Data

We used a UAV-borne LiDAR system mounted to a DJI Matrice 600 Pro payload at a 90° pitch angle, and same heading and roll as the UAV platform. The system included a discrete infrared LiDAR scanner (M8 sensor, Quanenergy Systems, Inc. Sunnyvale, CA, USA) and the corresponding industry standard inertial and navigation systems. In addition, we used a ground based differential Global Positioning System (dGPS, Trimble R8) during the UAV-LiDAR survey, set up in post-positioning kinematic (PPK) mode, which logged real-time satellite coverage (cf. Ravenga et al. 2022 [30] for details on the airborne and ground system). The coupling of the satellite coverage data with the UAV-based laser and navigation data produced allowed the generation of georeferenced point cloud data (PCD) scenes, following Davidson et al. (2019) [50]. We visualized the PCD scenes of barley and wheat crops at maturity stage in Figure 3 (a and b, respectively).

UAV-LiDAR data were acquired according to the planned UAV-LiDAR survey at a height of 40 m above ground level. Following a regular auto-pilot flight grid, we ensured a 20% overlap between individual LiDAR scans of ca. 50 m width and 250 pp/m^2 (cf. Revenga et al. 2022 [30] for additonal details on applied flight parameters). The surveys were conducted during May-July 2020, and during April-July 2021, coinciding with the two growing seasons.
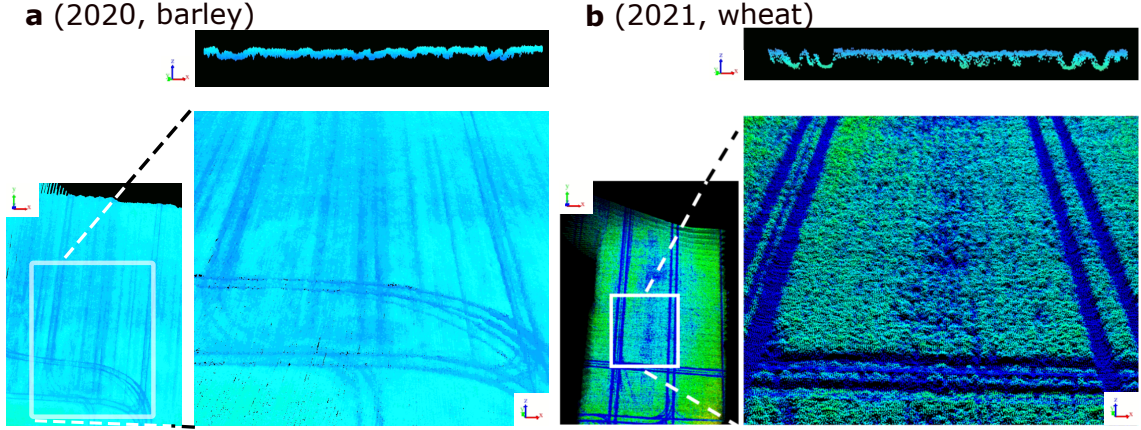
Figure 3. Point cloud data (PCD) scenes. The crops are portrayed at maturity stage. **a**: barley field, during 2020. **b**: wheat field, during 2021. The PCD scenes are colored by elevation. In both **a** and **b**, the upper panes show the cross section view of the PCD, with a buffer depth of 0.5 m. Axes x, y, and z, indicate easting, northing, and elevation, respectively. It can be noted a higher PCD porosity in **b**, than in **a**, corresponding to more sparse crops and lower AGB values.

2.3 Field Based Destructive Measurements of Aboveground Carbon

In order to acquire reference values of crop AGB (i.e. ground-truth labels) to provide supervision to the ML regression algorithms, AGB samples were systematically collected from the field at random locations during the growing season. The locations selected during sampling are visualized in Figure 4; the resulting data sets, size and dimensions, are described in Table 2.31. The AGB sampling procedure followed the ICOS protocol for ancillary vegetation measurements [51] in 2020. During 2021, this AGB sampling procedure was modified, in order to maximize data sample size and quality, with a limited fieldwork capacity. Therefore, in 2021, at each location, three adjacent individual samples were collected. In total, three separate data sets of AGB were produced (Table 2.31).

An additional AGB dataset in 2021 was produced, composed of *augmented* samples. The augmentation procedure consisted of adding adjacent AGB samples, and their corresponding UAV-LiDAR data samples, so that both the AGB label and the LiDAR counterparts could be recalculated from the resulting combined sample. This augmetation scheme is shown in Figure 4 (c). This procedure allowed to produce one larger dataset (specifically, with 4/3 times more data samples) at a spatial resolution of 0.35-0.52 m² (cf. Revenga et al. 2022 [30] for a detailed explanation of the augmentation procedure).

We considered the plant C content in two separate parts: (i) aboveground and (ii) root carbon components (AGC and $root_C$, respectively). AGB was harvested and measured at randomized locations within the study site, according to ICOS protocols [51], throughout the two growing seasons (Figure 4 shows the sampling locations of AGB). Then, the AGB samples were oven-dried for 72h at 65°, to assess the dry biomass weight. The plant C content was assessed by the ICOS Ecosystem Thematic Center (ETC) via basic laboratory analysis [51] from leaf tissue. This evaluation involved determining the C-to-AGB ratio at 16 locations, using 45g of tissue from the uppermost and middle-height leaves at each location. The resulting C-to-AGB ratios were 46.6 ±

0.3% for spring barley and 47.7 ± 0.3% for winter wheat. For simplicity, we assumed this ratio constant across the aboveground plant components. Using the AGB prediction results, and the C-to-biomass ratio measured, we calculated the total plant AGC.

Following, we converted the point-based AGC estimates to surface-based values, so that the resulting reference AGC values were resampled to 1 m² resolution. In such way, we obtained a distribution of surface-based ground-truth estimates of AGC density at a spatial resolution of 1 m². Table 1 provides a comprehensive overview of the sample count and spatial dimensions AGC reference labels in this study. The spatial distribution of the AGC sampling points is visualized in Figure 4 (b).

Table 1. Description of aboveground carbon (AGC) data sets. The subindex *aug.*, refers to the *augmented* dataset.

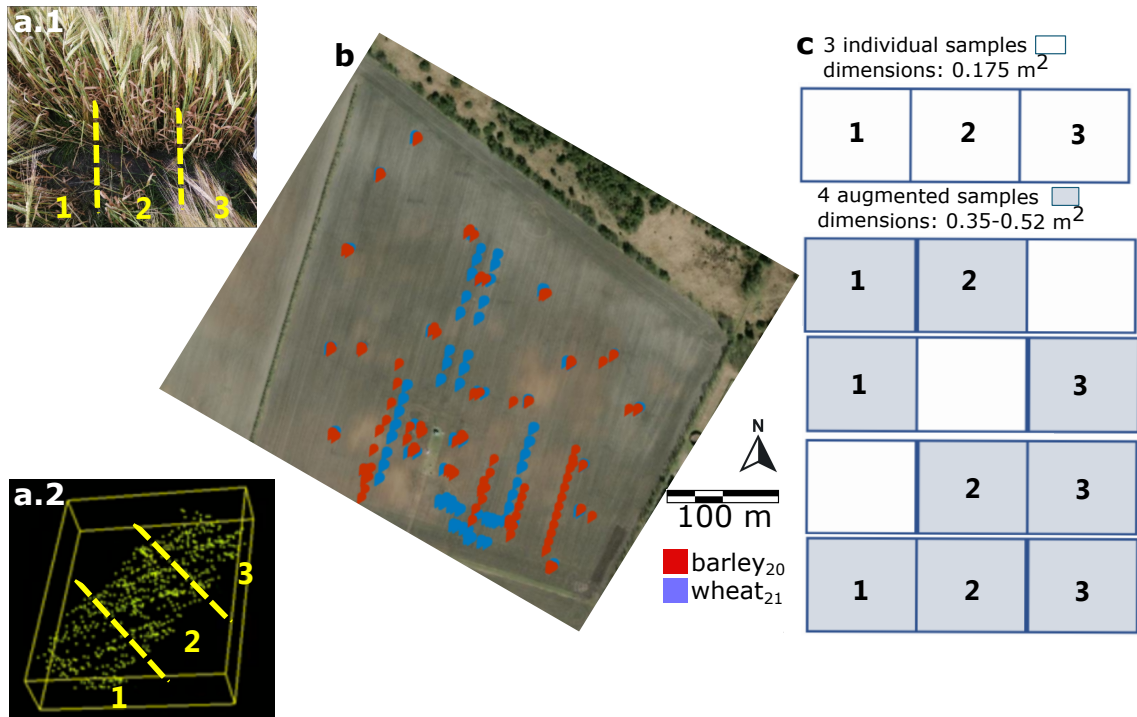| Growing season	Data set name	Number of samples	Sample dimensions (m)
2020	$barley_{20}$	104	1 x 0.35
2021	$wheat_{21}$	455	0.5 x 0.35
	$wheat_{21,aug.}$	609	(1-1.5) x 0.35

Figure 4. **a.1**: Three adjacent aboveground biomass samples (AGB) and the corresponding three LiDAR samples (**a.2**, dimensions of each sample: 0.5×0.35 m). **b**: The spatial distribution of the AGB sampling locations. Each color indicates one of the original data sets: **red**: barley samples collected in 2020 (i.e. $barley_{20}$); **blue**: wheat samples collected in 2021 (i.e. $wheat_{21}$). **c**: dimensions of three original AGB samples (above), and data augmentation scheme by permutation (below); i.e. adding either two or three samples).

2.4 Root and Soil Carbon Estimates

Unlike AGC, we did not assess $root_C$ based on direct measurements. Instead, it was estimated based on the sampled AGC, reference literature [52, 53, 54] and a linear dynamic allometric model based on the phenological growth stage [55].

The total plant C estimates (i.e. AGC plus $root_C$) were obtained by calculating at each point the total plant C derived from the AGC prediction. In order to obtain this estimate, we considered the allocation of $root_C$ as a function of the phenological stage using Eq. 1. We fixed $root_C$ at anthesis as $10 \pm 1\%$ of total plant C at maturity of crops, according to reference literature [52]. Therefore, $root_C$ was calculated as a function of (i) AGC, (ii) the rate at which GPP is translocated to the roots (GPP_{roots}) [53], and (iii) the phenological stage (i.e. x_{ph}) [55]:

$$root_C(x_{ph}) = \begin{cases} x_{ph} \cdot GPP_{roots}, & \text{if } x_{ph} < x_{anthesis} \\ (0.1 \pm 0.01) \cdot AGC_{mat}, & \text{if } x_{ph} = x_{anthesis} \\ root_{C,post}(x_{ph}), & \text{if } x_{ph} \geq x_{anthesis} \end{cases} \tag{1}$$

where AGC_{mat} indicates aboveground carbon at maturity stage; the function $root_{C,post}(x_{ph})$ was defined by a linear fit to $root_C$ at anthesis and values of GPP_{roots} reported in literature at each growth stage, for wheat and barley in sandy soils, respectively [53]. Similarly, GPP_{roots} was obtained as the slope of a linear fit between the onset of the season and $root_C$ at anthesis.

Lastly, we assessed the quantity of photoassimilated carbon translocated to the soil as rhizode-posits (i.e. $soil_C$). Our estimation of the soil carbon content relied on information from existing literature. In conventionally managed crop fields, $soil_C$ in sandy soils has been previously mea-sured using ^{14}C labeling and reported as a relative fraction of GPP [54, 56]. Therefore, $soil_C$ was calculated as a linear fit to the values reported in literature of ^{14}C labeling for barley and wheat, specific to sandy soils. This resulted on an average translocation of GPP to rhizodeposits of 2.73% and 1% for barley and wheat, respectively.

2.5 Flux Measurements and Calculation

The study site is equipped with state-of-the-art instrumentation complying with ICOS pro-tocols for a class-1 ecosystem station [48]. The equipment used for ecosystem flux measurements encompasses: an EC system constituted of Gill HS-50 sonic anemometers (Gill Instruments Ltd, Lymingdon, UK) and LI-7200RS enclosed infrared CO_2/H_2O gas analyzers (LI-COR, Lincoln, NE, USA) sampling at a frequency of 20Hz.

Additionally, the station is further equipped for air- and soil-meteorological monitoring, mea-suring the following variables: air temperature, relative humidity, air pressure, global radiation, photosynthesis active photon flux density, soil temperature, and soil water content [18].

Raw data processing

The raw data processing, quality control, and subsequent gap-filling procedures followed closely the standards applied by ICOS ETC [48, 57]. The EC data produced at DK-Vng became part of the ICOS ETC database only in 2021. For cosistency, in order to apply the exact same treatment

to the two datasets (i.e. 2020 and 2021), we processed the raw data in-house according to the ICOS ETC standards.

Raw 20 Hz wind, CO_2, water vapor, and sonic temperature data were processed utilizing the EddyPro v. 7.0.9 software (LI-COR, Lincoln, NE). Half-hourly turbulent scalar fluxes were calculated as the covariance between vertical wind speed and scalar variables (i.e. CO_2, H_2O, T). The processing included statistical tests for raw data screening [58], double coordinate rotation, block averaging, time-lag optimization to maximize covariance, compensation for the effect of density fluctuations on fluxes [59, 60], and low- and high-frequency spectral correction [61]. Half-hourly turbulent scalar fluxes were calculated as the covariance between vertical wind speed and scalar variables (i.e. CO_2, H_2O, T).

Post-processing: Spike Removal, Quality Control, and Gap Filling

During raw data processing and post-processing, low quality data were rejected, following a standard data screening procedure. This operation consists of two sub-tasks: (i) an absolute limit test, that sets boundaries for a physically plausible range of values, and (ii) individual outliers were detected following the method proposed by Papale et al. (2006) [62]. Additionally, data were removed when the wind came from the direction covering the instrumental plot (Figure 5, b), so we prevented the instrumentation from influencing the measurements.

The data rejected left therefore gaps in the datasets of both years. During 2020's growing season, this resulted in a 56.8% of data rejected after all three filtering tests were applied. While the gaps occurred mainly at the beginning and end of the 2020 year (Autumn and Winter), the growing season was better populated with valid NEE data values. The data were gap-filled according the method proposed by Reichstein et al. (2005) [63], and the u*-filtering procedure was based on season. The processing of the 2021 flux data set followed the same procedure as for the 2020 season. The processed data showed a missing ratio of 32.9% after the quality control test and de-spiking, showing fewer gaps than the previous year and also a better flux data recording during the growing season. To acquire a continuous dataset and allow for the estimation of cumulative carbon budgets, data gaps were filled following the method of Reichstein et al. (2005) [63], using the REddyProcWeb tool. The method combines lookup tables of average fluxes under comparable meteorological conditions in a certain time window. If meteorological measurements are missing, fluxes are estimated as the mean flux at the same time of the day in each time window (i.e. mean diurnal course).

A detailed description of the EC system, raw data processing and post-processing routines at this same EC station can be found in Jensen et al. (2017) [18].

Estimation of Flux Climatology Footprint

We calculated the flux climatology footprint using the model developed by Kljun et al. (2002) [64], and extracted the polygon covering the 70% influence around the station (Figure 5, a). The reason to select specifically the 70% area of influence around the EC station followed the criterion of maximizing the surface covered before reaching disruptions in the vegetation cover (e.g. hedgerow, gravel road), so it is ensured that the measured signal comes only from the vegetation. This allowed to make the surveyed area representative of different crop canopy structures, and to

benefit from the cancelling of statistical errors, through spatial averaging effects [30, 65], thereby
reaching optimal predictions of AGC at the footprint scale.

Furthermore, in order to remove the influence of the instrumental plot surrounding the EC
tower on the measurements, this area was masked out. For the 2020 dataset, the wind directions
that covered the instrumental plot (18–198°) were excluded of further processing. The wind directions excluded in 2021 differed slightly fro mthe previous year (the directions masked covered the
section 18–116°), as some instrumental modifications were required at the site (Figure 5, b.1 ad
b.2).
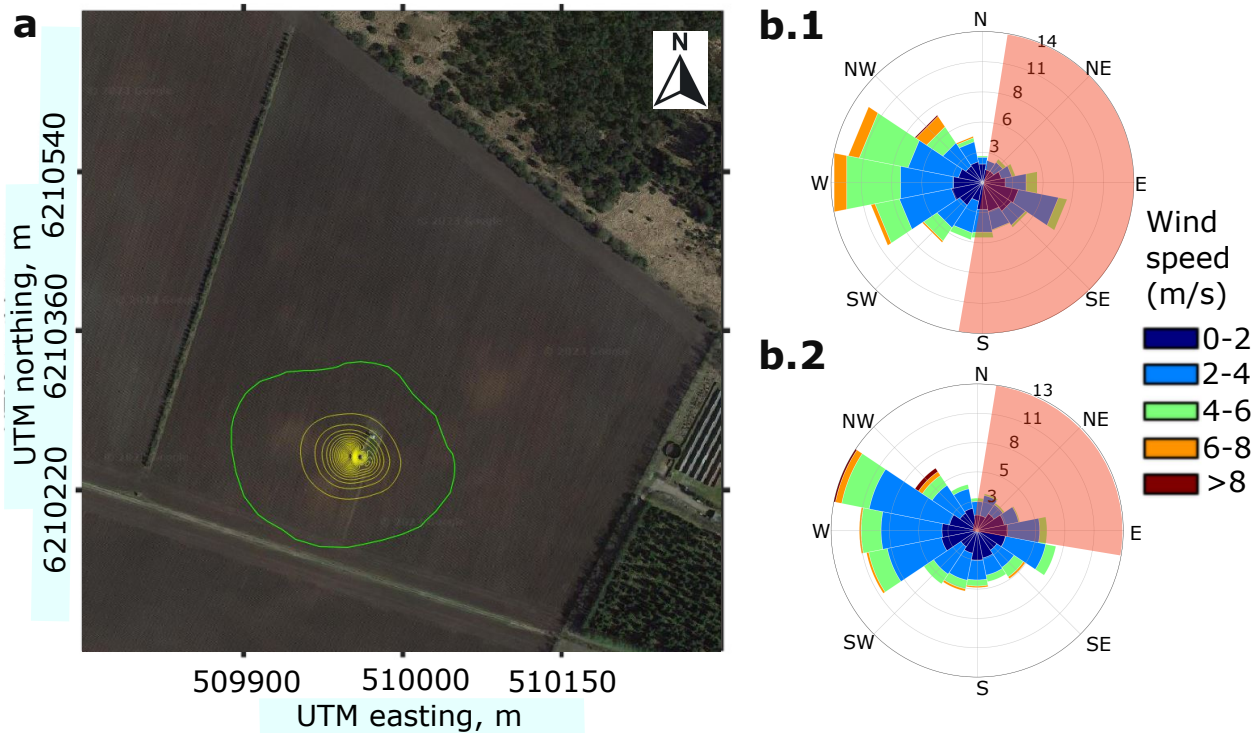
Figure 5. **a:** Flux footprint climatology map from the study site; the yellow contours indicate areas of
10 % increase of influence (source of background image: Google Earth 2023). **b.1, b.2:** wind frequencies
at the study site during April–August of 2020 and 2021, respectively. The radius indicates total frequency
of a given wind direction; the color indicates wind speed ($\mathrm{ms^{-1}}$). The shaded red areas cover the wind
directions influenced by the instrumental plot—which were filtered out for flux analysis.

²⁹¹ ***Ecosystem Flux Balance***

²⁹² After data processing, the flux data provide an estimate of the net ecosystem exchange (NEE)
²⁹³ (Figure 11, Annex I), allowing to estimate other NECB components. The estimation of net primary
²⁹⁴ productivity (NPP) involved calculating the difference between NEE and ecosystem respiration.
²⁹⁵ Therefore, we considered the flux balance

$$NPP = (-NEE) + R_h \approx (-NEE) + R_{soil} \tag{2}$$

²⁹⁶ where R_h accounts for the heterotrophic respiration, while the autotrophic plant respiration
²⁹⁷ is contained within NPP. As per the usual convention, the negative sign indicates flux direction
²⁹⁸ towards the ecosystem; the positive sign indicates a flux release towards the open atmosphere. In
²⁹⁹ conventional croplands (Figure 1), where the influence of higher-order heterotrophs (e.g. mammals,
³⁰⁰ birds) can be considered negligible, the microbial soil respiration (R_{soil}) constitutes R_h [66]. Here,
³⁰¹ we modeled R_{soil} as a function of soil temperature during winter. Following Lloyd and Taylor
³⁰² (1994) [67], a second-order polynomial was fitted to the measurements of NEE prior to the start
³⁰³ of the growing season (i.e. constituted of the R_h component only), as function of soil temperature
³⁰⁴ 5 cm below surface. We filtered out R_{soil} values corresponding to frozen conditions (i.e. < 0.5 °C)
³⁰⁵ for the model fit. Then, we extrapolated the modeled R_{soil} to the entire growing season.

2.6 Machine Learning-based Carbon Estimates

2.6.1 Training and Validation of Predictions

³⁰⁸ Three different ML regression models were initially selected for the task of AGC prediction.
³⁰⁹ They were calibrated on a training dataset, and their performances were evaluated on a separate
³¹⁰ validation dataset; then, the best performing one was chosen for testing. This procedure helped
³¹¹ avoid overfitting the model to the data, preventing an optimistically-biased accuracy assessment.

³¹² Therefore, we selected three fundamentally different ML methods; one representative of regu-
³¹³ larized linear models (i.e. Huber regressor) [68, 69], one tree-based ensemble method (i.e. Extreme
³¹⁴ Randomized Trees, ERT) [70], and one exemplar from the boosting methods (i.e. Extreme Gradi-
³¹⁵ ent Boosting, XGBoost) [71].

³¹⁶ The model performance on the validation set was assessed via the average performance (in-
³¹⁷ dicated by the overbar) of the following metrics over 10 randomized executions: coefficient of
³¹⁸ determination ($\overline{R^2}$), mean squared error ($\overline{MSE}$) and mean absolute error ($\overline{MAE}$). ERT obtained
³¹⁹ the best results across all four scores and therefore was selected as the model of choice. For more
³²⁰ details on the model selection, validation and test procedure cf. Revenga et al. (2022) [30].

2.6.2 Description of the Model Selected

³²² Extremely Randomized Trees (ERT) is an ensemble learning technique that aggregates the
³²³ results of multiple individually created decision trees to output, e.g. regression results. Originally
³²⁴ derived from the Random Forest model [72], in an ERT model every individual predictor—i.e.
³²⁵ a binary decision tree—is constructed from a random selection of features without replacement
³²⁶ from the whole training set. A single tree decides at each node, which split—of a random subset
³²⁷ of feature splits—reduces the reconstruction error (e.g. MAE or MSE) the most. The random

328 sampling of predictive features, plus the randomization step at each split node, leads to more
329 diverse and thus less correlated decision trees, thereby leading to improved generalization results,
330 and lower training times. Each tree is considered to be a "weak" regressor performance-wise but the
331 combination creates an ensemble that outperforms the individual regressors. As final prediction,
332 the average predictions of the individual decision trees in the forest is used, providing an estimate
333 of above ground carbon (i.e. $\widehat{AGC}$).

3 = Results =

335 The AGB sampling along 2020 and 2021 resulted in two distinct curves of AGB build-up
336 (Figure 6 a and b). While in 2020, a plateau of plant AGB was reached (by 1 July 2020), in 2021,
337 the turning point was not reached by the time of the last biomass survey date (14 July 2021). This
338 is mainly explained by harsher environmental conditions that the crops of 2021 endured at the
339 onset of the season (see Annex I). Interestingly, the shaded ribbon around the time series of AGB
340 in both years, covering the 68% confidence interval, is remarkably wider at the end of 2021's season
341 than at the end of 2020's season. This is consistent with a more open canopy structure (Figure 3)
342 corresponding to a more heterogeneous and sparser AGB density as well as lower total plant C
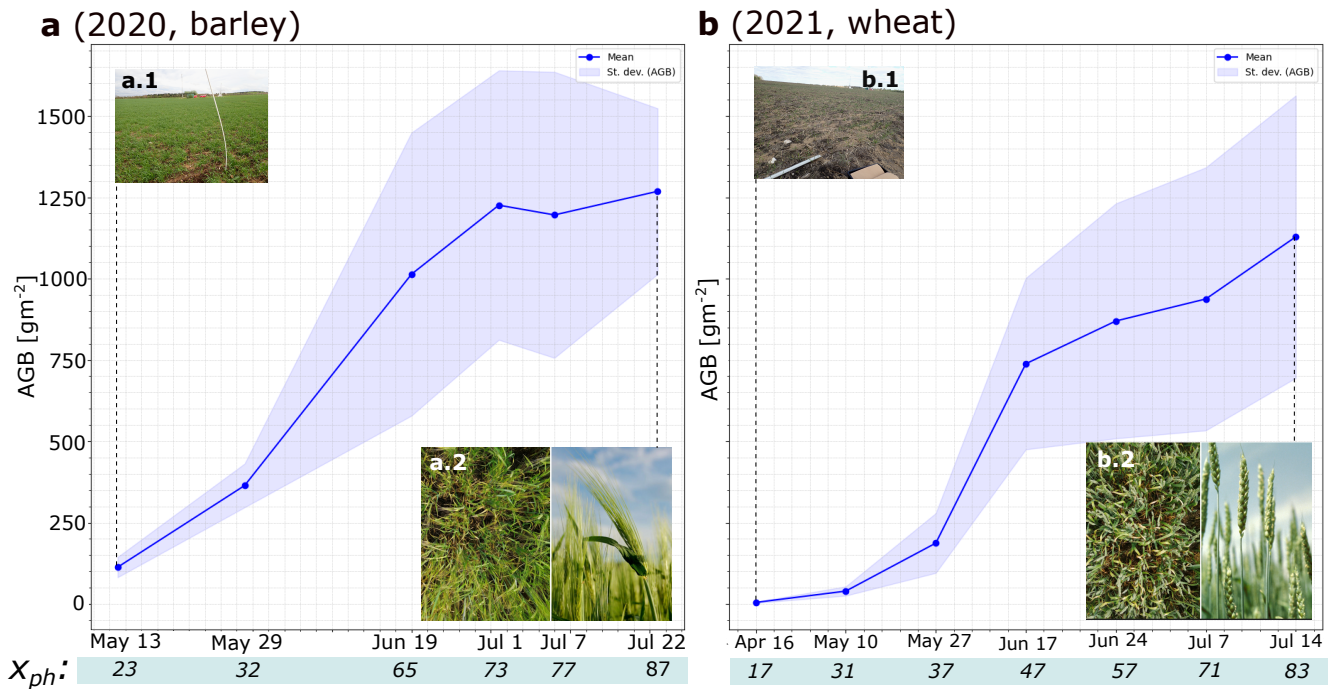343 accumulation.

Figure 6. Crop development along the two growing seasons considered. Aboveground biomass (AGB) development during 2020 (**a**, barley) and during 2021 (**b**, wheat) growing seasons, respectively, indicating the dates of AGB sampling events. Y-axis indicates dry AGB matter. The blue solid line indicates the mean per sampling campaign, while the shaded area covers $\pm$ the standard deviation. **a.1, a.2:** spring barley crop structure at the start of the sampling campaign and at maturity stage, respectively. x_{ph}: phenological growth stage (Zadoks decimal code) [55]. **b.1, b.2:** winter wheat crop structure at the start of the sampling campaign and at maturity stage, respectively. The AGB sampling during 2021 started earlier than in 2020, hence an initial value close to 0 at the start of the 2021 season.

3.1 Plant Biomass and Carbon Maps via UAV-LiDAR

The best performing regression model (ERT) resulted in a prediction performance of $\overline{R^2}$: 0.72, $\overline{RMSE}$: 227 g, $\overline{MAE}$: 121 g at a spatial resolution of 1 m², on the validation sets, and the model was not overfitted. ERT outperformed the other two candidate models: XGBoost ($\overline{R^2}$: 0.67, $\overline{RMSE}$: 250 g, $\overline{MAE}$: 182 g) and Huber regressors ($\overline{R^2}$: 0.70, $\overline{RMSE}$: 237 g, $\overline{MAE}$: 190 g). Thus, ERT was selected for AGB and AGC prediction. For further details in feature selection and specific information related to the processing pipeline, the reader is referred to Revenga et al. 2022 [30].

Therefore, via the spatially-resolved regression outputs of the ERT model, we obtained surface-based maps of AGB and AGC. We visualized the AGB and AGC predictions based on the input UAV-LiDAR point cloud data at 1 m² resolution in Figure 7. The values shown present a confidence interval of 68% of 108 gAGC/m² in barley, and 134 gAGC/m² in wheat, corresponding to 1 standard deviation over 10 random executions of the ERT prediction on the test sets (following the procedure described in Revenga et al., 2022) [30]. We selected nine UAV-LiDAR survey dates (five during 2020; four during 2021), and intersected them with the 70% of the area of influence surrounding the eddy-covariance station to visualize the spatially-resolved model output.
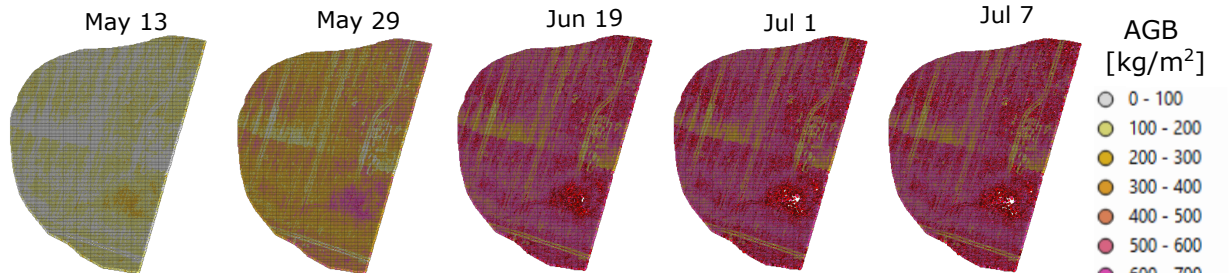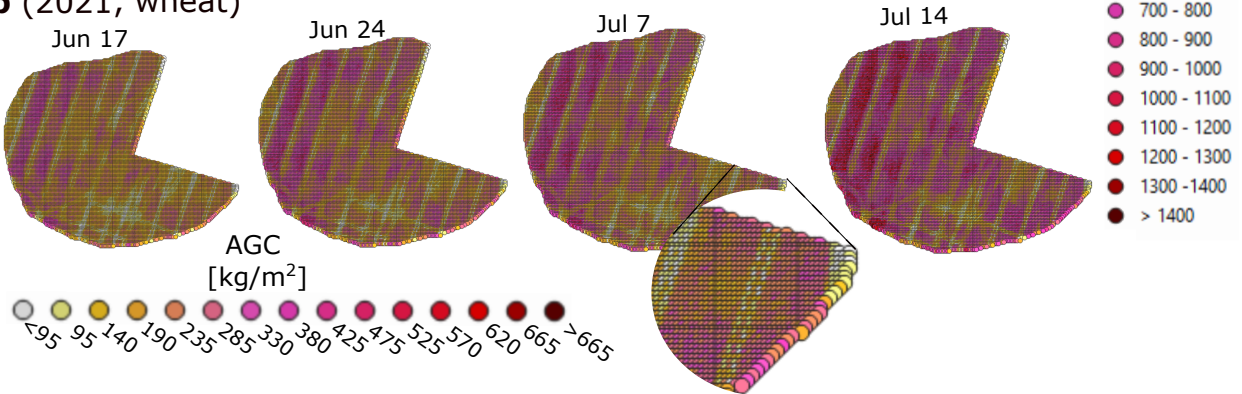

Figure 7. Exemplary aboveground biomass (AGB) and aboveground carbon (AGC) maps. **a:** 2020 growing season; **b:** 2021 growing season. Values in legend indicate predictions of dry AGB matter and the corresponding AGC value. A sector of the eddy covariance station footprint was clipped out to avoid influence from the instrumental plot on the results: in 2020, the (18–198)° wind directions were excluded; in 2021, the wind directions (18–116)° were excluded. Both legends share the same color gradient since AGC is modeled as a linear function of AGB.

Temporal Development of Biomass and Carbon

In 2020, the AGB collection campaign started at a level of 100 gm^{-2} of AGB. In Figure 6 (**a**) it can be observed a steady increase until 1 July, where there is a turning point, and a saturation plateau afterwards. From then onward, AGB stabilizes, i.e. by the harvesting date (end of July), the AGB are just slightly above the one measured on 1 July.

In contrast, in order to extend the span of AGB measurements, during the 2021 campaign the AGB sampling started at a point slightly above 0 gm^{-2}, where can be noted a slow start of AGB accumulation. By approximately the same date (27 May), the AGB in 2021 growing season lags 150 gm^{-2} behind the previous year. This can be compared with the NEE of both years (Figure 11, in Annex) showing a "false start" in 2021 11 (b), so until start of June NPP barely offsets R$_{eco}$. Instead of saturating by 1 July, AGB kept growing until the last sampling date. This observation was expected, considering that the crops in 2021 exhibited a time-lag of approximately 15 days compared to the previous year (see Figures 11 and 12, in Annex).

The difference in AGB between the two years translates linearly to differences in AGC by modeling C content to be constant across all plant tissue ($46.6 \pm 0.3\%$ in barley, and $47.7 \pm 0.3\%$ in wheat). Notably, wheat moves a slightly greater amount of photoassimilated C below ground compared to barley, in relative terms (Figure 8) [53]. This different strategy becomes increasingly evident as the growing season progresses and becomes particularly apparent at the maturity stage. The difference between the measured AGC in both growing seasons (i.e. $\approx$ 235 gm^{-2} more in 2020 than in 2021) can be attributed to the harsher environmental conditions that the 2021 crops endured at the beginning of the season, causing a delay and a sparser crop structure (see Annex I).

Above- and Belowground Carbon Estimates

We took the AGC assessment as the reference component, and modeled the belowground C component (i.e. root$_C$ and C translocated to the soil as rhizodeposits), according to reference literature [53, 52], and penology dependant allometry (Eq. 1). Figure 8 (a) shows the percentage of GPP translocated to above- and belowground components during the crops' lifecycle. Similarly, Figure 8 (b) shows the actual C stocks estimated (as a percentage of the total plant C), both in above- and belowground components. The values shown result from averaging the percentages reported in reference literature of isotope C pulse labeling, for the same crop type under similar soil and climatic conditions. They do not include C transfer to the soil as rhizodeposits.
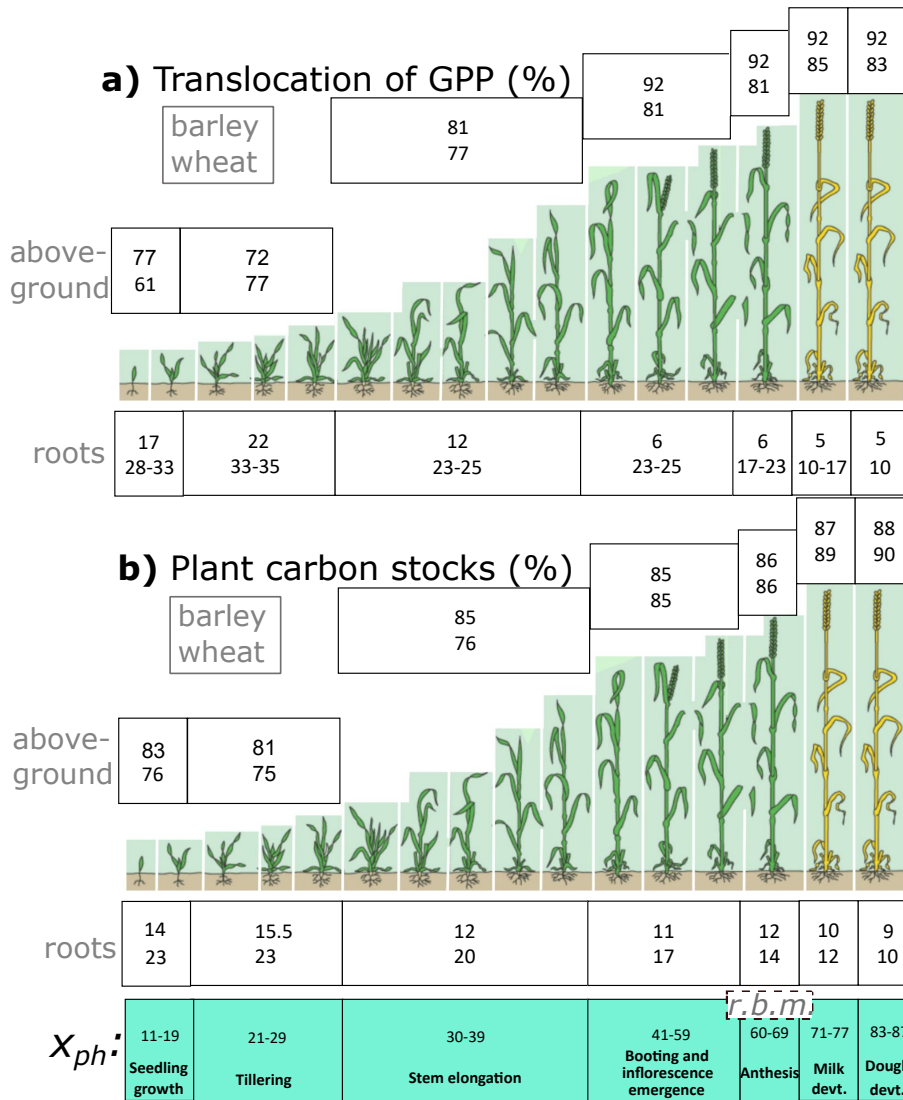
Figure 8. **a:** Translocation of photoassimilated atmospheric carbon (i.e. GPP) to aboveground and root components (rhizodeposits are not included); values in white boxes indicate estimated % corresponding to the same phenological growth stage. **b:** Plant carbon stocks along the growing season showing the estimated carbon allocation at each phenological stage (adapted from Large et al., 1954) [73]. Percentage values of carbon in roots (both translocated and stocked) are derived from Kuzyakov et al. 2000 [53] for wheat and barley crops in sandy soils. Each white box shows values for spring barley (above) and winter wheat (below). x_{ph}: phenological growth stage (Zadoks decimal code) [55]. The inset indicating r.b.m. shows the stage when the root biomass maximum occurs.

3.2 Carbon Flux via the Eddy-Covariance Method

The cumulative NPP curves of the two growing seasons considered are shown in Figure 9. The trajectory of the NPP curve in the year 2020 exhibits an early start (by beginning of May), and reacing the saturation point by the last UAV-LiDAR survey (i.e. on July 22). In contrast, in 2021, NPP starts to grow visibly by ca. May 20. Moreover, the last survey conducted in 2021 (i.e. July

14) coincides with a phase characterized by the ongoing upwards trajectory of the net ecosystem's uptake.

It can be observed a general favorable agreement between the two methods, with a slight underestimation of the UAV-LiDAR assessment at the end of 2020, and a slight overestimation towards the end of the 2021 season.
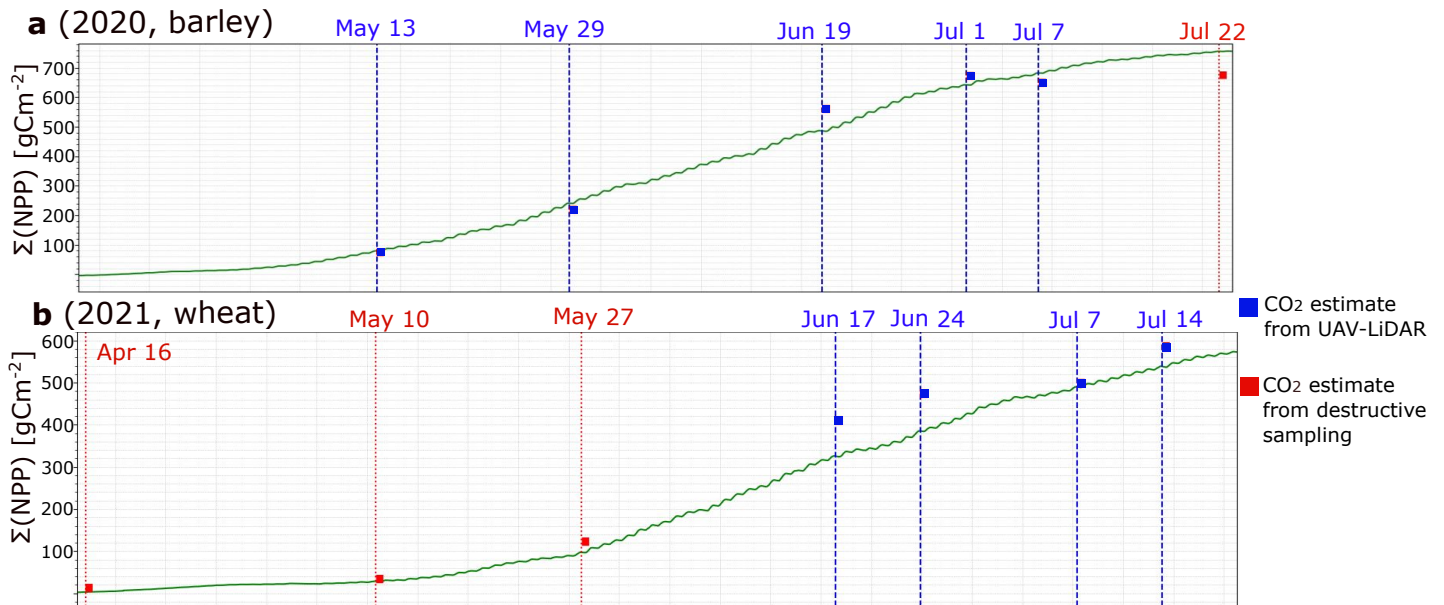

Figure 9. Cumulative NPP (gCm^{-2}) along (**a**) the 2020 and (**b**) the 2021 growing seasons (green curve). The red dotted vertical lines indicate aboveground biomass (AGB) sampling dates, while the blue dashed lines indicate dates in which both AGB sampling and UAV-LiDAR surveys took place. The square marks indicate the plant-C estimates for a given date using the UAV-LiDAR method (blue dates), or based on C estimated from destructive sampling (red dates).

3.3 Comparing Flux Data and Plant Carbon Estimates from UAV-LiDAR

We partitioned the different components of C uptake shown in Figure 9. This resulted in a per-component estimate of C stocks along the growing seasons (Table 2). The results allow a comparison of the plant C estimates via the UAV-LiDAR method against the cumulative partitioned fluxes estimated via the eddy covariance method.

Table 2. Results of carbon estimates via the two independent methods considered. The first column indicates the UAV-LiDAR survey dates; second and third columns show the plant carbon stock estimated via the UAV-LiDAR method (both AGC and $root_C$); the last three columns show the cumulative values (from the start of the photosynthetic season) of the ecosystem flux components partitioned into net ecosystem exchange (NEE), heterotrophic respiration R_h and net primary productivity (NPP). x_{ph} indicates the average phenological growth stage (Zadoks decimal code) [55] measured at 12 control plots. $soil_C$: rhizodeposits.

Method		UAV-LiDAR			eddy covariance		
d/m/yyyy	x_{ph}	**AGC** $[gm^{-2}]$	**root**$_C$ $[gm^{-2}]$	**soil**$_C$	**-NEE** $[gCm^{-2}]$	**R**$_h$ $[gCm^{-2}]$	**NPP** $[gCm^{-2}]$
13/5/2020	23	52.4	8.9	1.72	35.7	143.4	91.0
29/5/2020	32	168.8	32.0	5.63	81.9	237.9	252.5
19/6/2020	65	469.3	65.2	15.0	286.1	423.0	497.7
1/7/2020	73	567.5	75.1	18.0	401.4	533.1	653.8
7/7/2020	77	553.6	66.4	17.4	423.6	577.7	693.7
22/7/2020	87	587.3	58.7	18.1	463.4	681.8	767.6
16/4/2021	17	2.3	0.7	0.0	83.6	90.7	0.9
10/5/2021	31	18.4	5.5	0.3	147.6	100.8	25.5
27/5/2021	37	86.7	25.8	1.1	68.6	229.5	94.5
17/6/2021	47	341.9	55.5	4.0	102.5	418.4	321.3
24/6/2021	57	402.7	58.0	4.7	144.3	482.0	372.5
07/7/2021	71	434.1	50	4.9	227.3	592.1	486.1
14/7/2021	77	522.6	48.5	5.8	251.5	672.1	532.0

Furthermore, we conducted a method inspection, in order to quantify the degree of convergence between the UAV-LiDAR-based method and the flux-based method. This aalysis allowed us to observe the general degree of agreement between the two tecniques, as well as to spot sources of inconsistency. To that end, we used the following metric, referred to as delta-ratio (Δ_C). It is defined as the ratio between the increment of plant C and the increment in NPP between two separate surveying dates:

$$\Delta_C = \frac{\Delta(NPP_{i,j}) - \Delta(PlantC_{i,j})}{\Delta(NPP_{i,j})} \cdot 100 \qquad (3)$$

where the subindexes i, j refer to two different surveying dates. The results of this analysis are visualized in Figure 10.
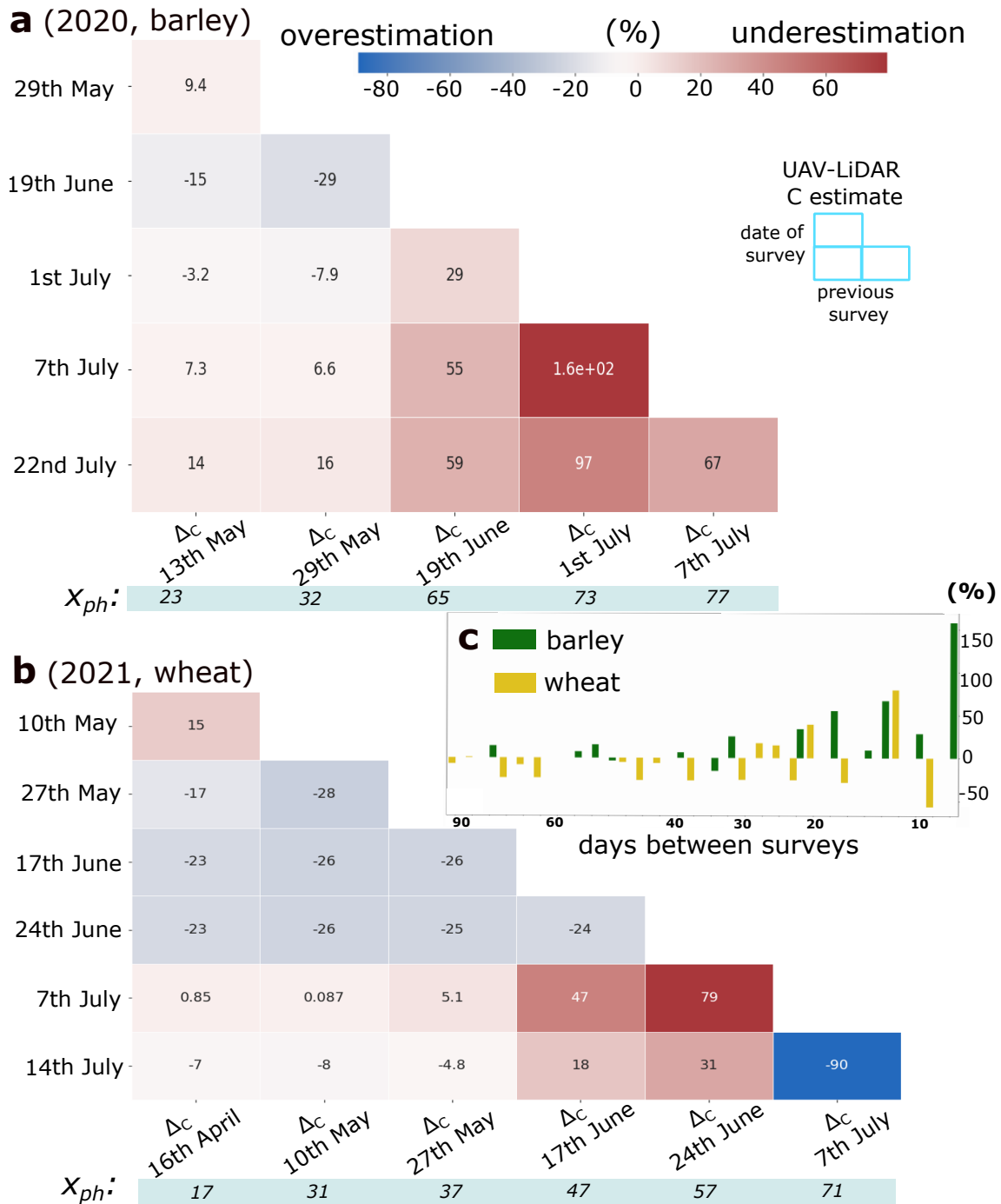
Figure 10. Carbon delta-ratio (Δ_C) values between pairs of surveying dates during the 2020 **(a)** and 2021 **(b)** growing seasons; the reference ($\Delta_C = 0\%$) is the cumulative NPP at a given date. The inset **(c)** shows the error distribution along the time between UAV-LiDAR survey dates for both crop types. It can be noted that (i) LiDAR estimates become more in agreement with NPP as time between surveys increases, and that (ii) considerable over- and underestimates are found between closely spaced dates during a late phenological stage (right tails of both **a** and **b** tables). x_{ph} indicates the average phenological growth stage.

⁴¹⁴ **4 = Discussion =**

⁴¹⁵   This study proposed a new method to acquire estimates of cumulative plant C stocks in
⁴¹⁶ cereal croplands using UAV-LiDAR and ML regression methods. The method presented was eval-
⁴¹⁷ uated by comparing results against the cumulative NPP values measured via the eddy-covariance
⁴¹⁸ technique—i.e. the current state-of-the-art for ecosystem flux monitoring at the ecosystem scale.
⁴¹⁹ The favorable match between the UAV-LiDAR estimates and the cumulative NPP, obtained via
⁴²⁰ the eddy-covariance method, indicate that the crop C dynamics can be captured accurately with
⁴²¹ reliance on minimal mobile instrumentation. This finding is specially apparent when the first UAV-
⁴²² LiDAR survey date is taken early in the growing season. Conversely, comparisons lose consistency
⁴²³ when time intervals between surveying dates are short, concurrently with a late phenological stage.

⁴²⁴ **4.1 Plant Carbon Components from UAV-LiDAR: Values and Uncertainty**

⁴²⁵   The values of AGC obtained via the spatially-resolved predictions of the ERT model, taking
⁴²⁶ UAV-LiDAR data as input were satisfactory at 1 m^2, and optimal at the flux footprint scale, due
⁴²⁷ to spatial averaging effects [30, 65]. We consider AGC as the component most accurately assessed
⁴²⁸ between the above- and belowground components. AGC was assumed linear with respect to AGB,
⁴²⁹ following a constant ratio of $46.6 \pm 0.3\%$ of C-to-AGB in barley and $47.7 \pm 0.3\%$ in wheat, obtained
⁴³⁰ via laboratory analysis. Therefore, the uncertainty estimate of the AGC component was assumed
⁴³¹ to be virtually the same as for AGB. While certain reference studies report of uneven C-to-AGB
⁴³² ratios across the plant components—e.g. leaves, root, grain bearing organs— [74], for simplicity, we
⁴³³ assumed this ratio to stay constant across the plant components. Furthermore, the uncertainty on
⁴³⁴ the lab analysis' results (i.e. $\pm 1\%$ of C-to-AGB ratio) is comparatively negligible with respect to
⁴³⁵ the uncertainty derived from the provision of ground-truth instances (i.e. the noise contained in the
⁴³⁶ AGC labels) [75, 76]. Such AGC label noise is an unavoidable source of error, as it represents the
⁴³⁷ uncertainty of the provided reference values of AGC. We characterised it as the standard deviation
⁴³⁸ of its distribution, and quantified it as 27.6% in barley, and 34.0% in wheat (details regarding this
⁴³⁹ quantification of error are given in the Appendix of Revenga et al. 2022) [30].

⁴⁴⁰   With respect to the belowground components of the estimated C stocks, some observations
⁴⁴¹ must be made. Management practices and environmental factors affect the root:shoot allometric
⁴⁴² ratio in cereal crops [52], and consequently alter this important sink of photoassimilates into the
⁴⁴³ ground [77, 78]. Therefore, such BGB estimates can be prone to bias or result largely uncertain [52].
⁴⁴⁴ Moreover, $root_C$ is much depending on soil water content, nutrient availability [79], as well as the
⁴⁴⁵ phenological growth stage (as visualized in Figure 8). In fact, there is high variability in $root_C$
⁴⁴⁶ along the growing season, increasing steadily towards the flowering period (i.e. anthesis), and then
⁴⁴⁷ gradually decreasing towards maturity [53], as nutrients are remobilized towards the developing
⁴⁴⁸ seeds during the last developmental stages, sourcing from the senescing components (e.g. roots) [80,
⁴⁴⁹ 81]. Here, in order to address this caveat, following the review by Hu et al. (2018) [52], we estimated
⁴⁵⁰ the BGB at anthesis (which corresponds to the root biomass maximum in Figure 8), as given by
⁴⁵¹ the ratio $\frac{root_C}{(AGC+root_C)} = 0.10 \pm 0.01$. This ratio relates AGC at maturity and $root_C$ at anthesis,
⁴⁵² standardized to 25 cm soil depth. This ratio holds for conventional farming systems and is also
⁴⁵³ supported by independent studies [82]. For barley, the absolute root biomass modeled at anthesis
⁴⁵⁴ aligned tightly with empirical studies on root biomass [77]. The phenological growth stage [55]
⁴⁵⁵ indicating anthesis was observed on 18 June 2020. Similarly, in 2021, the anthesis stage was
⁴⁵⁶ estimated to correspond to 1 July 2021. Following this ratio, and the rate of photoassimilated C

translocated to roots for barley and wheat in sandy soils [53], we estimated the $root_C$ component at each biomass sampling date. Therefore, one limitation of our method lies in the assumption that we estimate per-component C stocks based on the reported distribution of C in the existing literature for the same crops under similar conditions. At all events, we assumed that the ratios reported in reference literature [52] are robust and applicable to the environmental conditions and management type of the crops investigated in our study.

We consider that our results present limitations with respect to the design of the AGC sampling campaigns. The sampling design was conceived to optimize predictability of AGC from the LiDAR-derived PCD data, however, our sampling design turned out to be suboptimal for the application of comparing entire plant C and flux-based estimates on individual dates. Ideally, for the task of intercomparison of C stocks, at every date the locations selected for AGC sampling should be entirely randomized, across an area which is (i) large enough, and (ii) either within the flux tower footprint or representative of the vegetation traits contained within the footprint. However, during biomass data collection, in specific dates it was deemed advantageous for predicting *in situ* AGC to collect data from locations with contrasting AGB values. This approach allowed us to capture the two-dimensional variability of AGC corresponding to the observed variations in the PCD scene. While this procedure facilitated observing an empirical relationship between covariates (e.g. height metrics derived from PCD) and the response variable (i.e. AGC), it compromised the comparability of cumulative fluxes on particular dates. Our sampling design aimed at covering the tail ends of the joint probability distribution of covariates and the response variable. However, unintentionally, it introduced a bias when considering pairwise comparisons between specific dates. Consequently, this led to significant over- or underestimation of plant carbon stocks derived from UAV-LiDAR data in relation to net primary productivity (NPP), on certain dates. In both years, this is particularly evident in the comparison of Δ_C stocks when 7 July is involved (Figure 10). In Table 2, it can be observed how, on 7 July 2020, the AGC sample is 14 g lighter than the previous survey date (i.e. 1 July), while the cumulative NPP for the corresponding time period exhibits an increase of approximately 40 g. This corresponds to a decreasing LiDAR-derived plant-C estimate between these two dates (Figure 9, a). This disagreement can only be attributed to the inherent bias introduced by the sampling procedure. This stress this observation to highlitght the significant impact of the sampling design on the resulting outcome. Ideally, during each AGB sampling date, data collection should be completely randomized, without intervening explicitly to ensure AGC variability. On certain dates, the presence of sample selection bias [75, 76] introduced by the aforementioned approach resulted in inconsistency when comparing plant C values with flux-based cumulative carbon estimates. This is outcome is reasonable, as the continuous flux-based carbon estimates are independent and therefore unaffected by the AGC sampling design.

4.2 Ecosystem Carbon Uptake Derived from Flux Data

With respect to the modeled NPP, some observations should be made in the light of the presented results. Here, we modeled R_{soil} as a function of soil temperature, taking as sample data to model it the dates prior to the onset of the photosynthetic season (i.e. December–February). However, during these dates, air and soil temperatures did not span a wide range, staying close to frozen conditions. Therefore, the low dynamics in the values of soil temperature during the beginning of the year may have led to underestimations in the modeled R_{soil}. Accurately modeling heterotrophic soil respiration as a function of temperature may be challenging, particularly when the range of temperatures before shoot emergence (i.e. onset of photosynthetic season) is narrow.

This can lead to added uncertainties in the predicted values of R_{soil}. In order to narrow this uncertainty source down, further studies should consider combining the setup we employed with soil gas flux measurements. Additionally, the exact dates of fertilizer deposition by the land managers remain unknown. The effect of such field management (e.g. fertilizer application, irrigation) cannot be reflected in the LiDAR derived C estimates, but do have an impact on the measured fluxes, e.g. enhancing R_{soil} upon application of organic fertilizers.

4.3 Comparing Flux Data and Plant Carbon Estimates from UAV-LiDAR

Figure 10 shows the result of the comparison of C stocks obtained via the two independent methods, i.e. the UAV-LiDAR method and the flux-based method. The results indicate a degree of convergence between the two independently obtained estimates, and are shown as delta values (Δ_C, Eq. 3). Several observations can be made from these results:

- (i) The optimal reference date for comparing the increase in plant C stocks is the first day of the growing season, and this observation holds true for both years. When considering the 1st date as the reference, the mean error of predictions is the lowest obtained. In 2020, it is $2.5 \pm 10.4\%$, and in 2021, it is $-9.0 \pm 13.3\%$. These consistent results across both seasons indicate that this experimental setup is the best-performing. When using the 2nd date as the reference, the mean error between independent estimates in 2020 is $-3 \pm 16.9\%$, and similarly, in 2021, it is $-8.9 \pm 11.4\%$. If we take the 3rd date as the reference for comparison, the findings in 2020 indicate a persistent underestimation of $47.6 \pm 13.3\%$. In contrast, the results for 2021 exhibit a closer approximation to the reference NPP value, with a deviation of $-12.7 \pm 13.3\%$.

- (ii) The right tail ends of both tables, denoting UAV-LiDAR surveys during the late season, reveal that comparing increments in C between closely spaced dates at a late phenological stage leads to noticeable over- and underestimates. Therefore, besides the temporal proximity of survey dates, the phenological stage of the crops appears to exert a significant influence in the cumulative C stock predictions.

- (iii) In Figure 10, the inset panel (c) illustrates the Δ_C values of both crops over the temporal interval between survey dates (in x-axis). A clear trend can be observed, revealing a consistent increase in errors as the UAV-LiDAR survey dates become closer. This observed pattern in both growing seasons suggests that, irrespective of the crop type, estimates from surveys conducted in close temporal proximity tend to be suboptimal.

The observed disparities between the two methods considered fall within the uncertainty reported in reference studies between modeled and empirical approaches to estimate C stocks in croplands. For instance, a 18% of discrepancy between modeled and observed crop mass is reported by Soltani et al. (2012) [83]. However, we consider that the most noteworthy aspect of the proposed method is its ability to provide flexible estimates of C fluxes that align well with the EC flux estimates, and require minimal mobile instrumentation. Since the UAV-LiDAR estimates can be obtained without reliance on ground-based instrumentation, they enable assessments of C fluxes in agroecosystems that remain to date inaccessible and therefore poorly documented.

5 = Conclusions =

In this study, we developed and evaluated a method to estimate plant C stocks in managed cereal croplands, using UAV-LiDAR and machine learing (ML) regression methods. We benchmarked the results obtained by comparison with the corresponding cumulative NPP during the exact time period. From the obtained results, we conclude that total plant-mediated C stocks can be accurately estimated using UAV-LiDAR in combination with ML regression methods at the ecosystem scale. These estimates correspond to cumulative CO_2 fluxes uptaken during the crop development. The match between the temporal development in CO_2 uptake within the footprint of the eddy covariance station, using the UAV-LiDAR based method, and the eddy covariance estimates showed an optimal mean error of 2.5 ± 10.4 % in spring barley. In winter wheat, the optimal mean error was -9.0 ± 13.3 %. These findings indicate that the comparisons of C stocks over the entire growing season, considering the first survey as the reference date, were the most accurate.

However, the results also show that it is crucial to consider that UAV-LiDAR estimates of CO_2 uptake may exhibit substantial over- or underestimation under certain conditions, which should not pass overlooked by further research studies or practitioners. This can occur when (i) LiDAR surveys are too close to one another, particularly during the later stages of phenological development, and (ii) a sample selection bias is introduced. Therefore, care must be taken as regards allowing suitable time intervals between surveys and appropriate AGC sampling schemes. When comparing the resulting plant C values with eddy covariance estimates, a satisfactory level of agreement is observed, provided that the effects of AGC sampling design and time interval between UAV-LiDAR survey dates are taken into account.

We consider these results a promising step towards the data-driven upscaling of directly measured fluxes during the growing season in managed ecosystems, as well as towards the interpolation of CO_2 fluxes across eddy covariance stations by leveraging mobile platforms, LiDAR technology and ML regression methods.

6 = Author contributions =

7 = Acknowledgements =

8 = Funding =

9 List of abbreviations

- AGB: aboveground biomass.
- AGC: aboveground carbon.
- EC: eddy covariance.
- ECB: ecosystem carbon balance.
- ERT: extreme randomized trees.
- GHG: greenhouse gas.
- GPP: gross primary productivity.
- ICOS: integrated carbon observation system.
- LiDAR: light detection and ranging.
- ML: machine learning.
- NECB: net ecosystem carbon balance.
- NEE: net ecosystem exchange.
- NPP: net primary productivity.
- PCD: point cloud data.
- R_a: autotrophic plant respiration.
- R_{eco}: ecosystem respiration.
- RF: random forest.
- R_h: heterotrophic respiration.
- $root_C$: carbon content in roots.
- Rsoil: microbial soil respiration.
- RS: remote sensing.
- $soil_C$: soil rhizodeposition.
- UAV: unstaffed aerial vehicle.
- WDI: water deficit index.
- X_{ph}: crops growth stage (according to Zadoks decimal code).

10 Annex I: NEE, NPP, GPP, R_{eco} in both growing seasons (2020 and 2021)

Figure 11 displays the processed NEE over time for both years, with a 30-minute pixel resolution. It can be noted that in the 2020 season, there was an advancement of approximately 15 days, and more concentrated C uptake hotspots between 11:00 and 14:00 in late June and late July compared to the 2021 season.

Remarkably, in Figure 12, it can be observed that the time series of cumulative NPP and R_{eco} never cross each other in 2021 (b), while they do so in 2020 (a). The enclosed area under these two curves indicates the rate of C accumulation efficiency with respect to ecosystem respiratory

losses. It makes sense that in a more homogeneous, densely populated crop, the C uptake was
more efficient than in the sparse crops of 2021.

These observations are consistent with the AGC sampling campaigns—where more sparse
crops were sampled in the second year—and with the PCD representation of the cropfields (Figure
3)—where a higher PCD porosity was found in the second year as well as a lower cumulative NPP
flux (Figure 9).

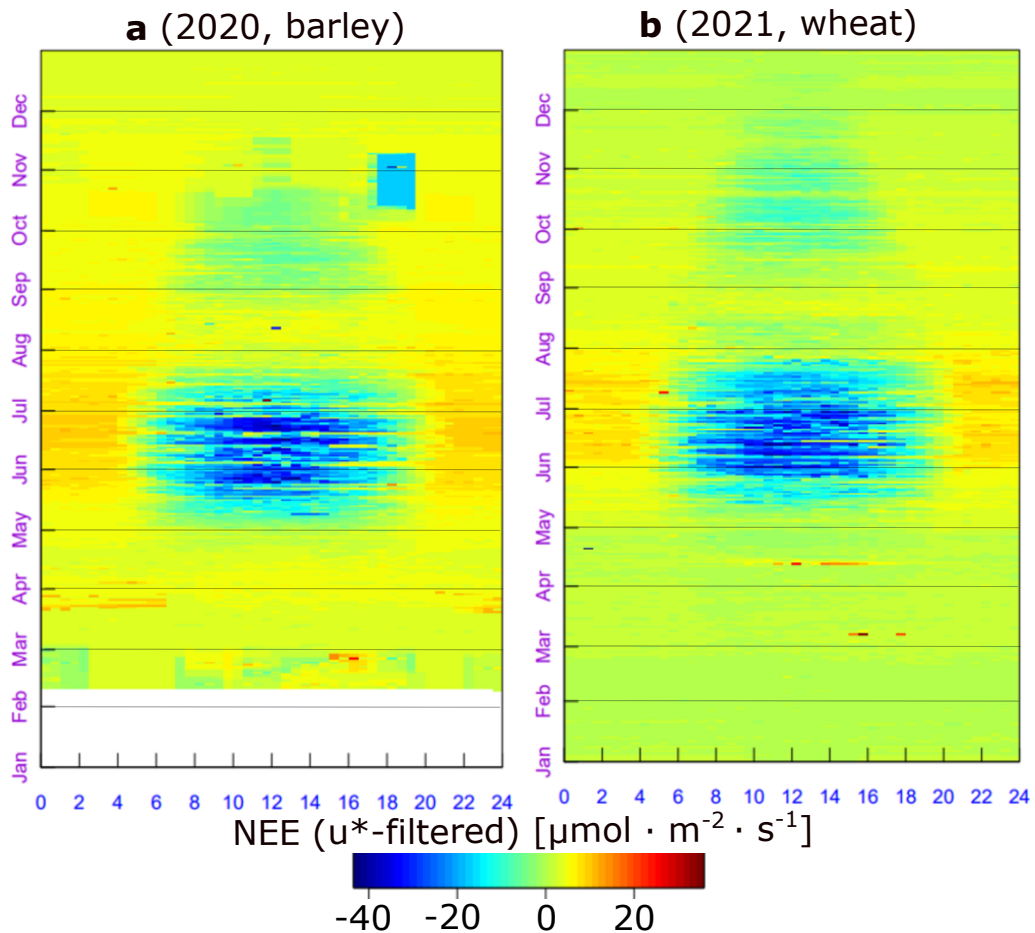**Figure 11.** Measured net ecosystem exchange (NEE) at Voulundgaard research station during 2020 (**a**)
and 2021 (**b**). Data displayed were gap-filled, spikes removed and u*-filtered. It can be noted a delay in
the onset of the growing season in 2021 with respect to 2020 of almost 3 weeks, including a false start in
mid May, partly explained by the cold spell of 10-12th February (figure obtained from the REddyProcWeb
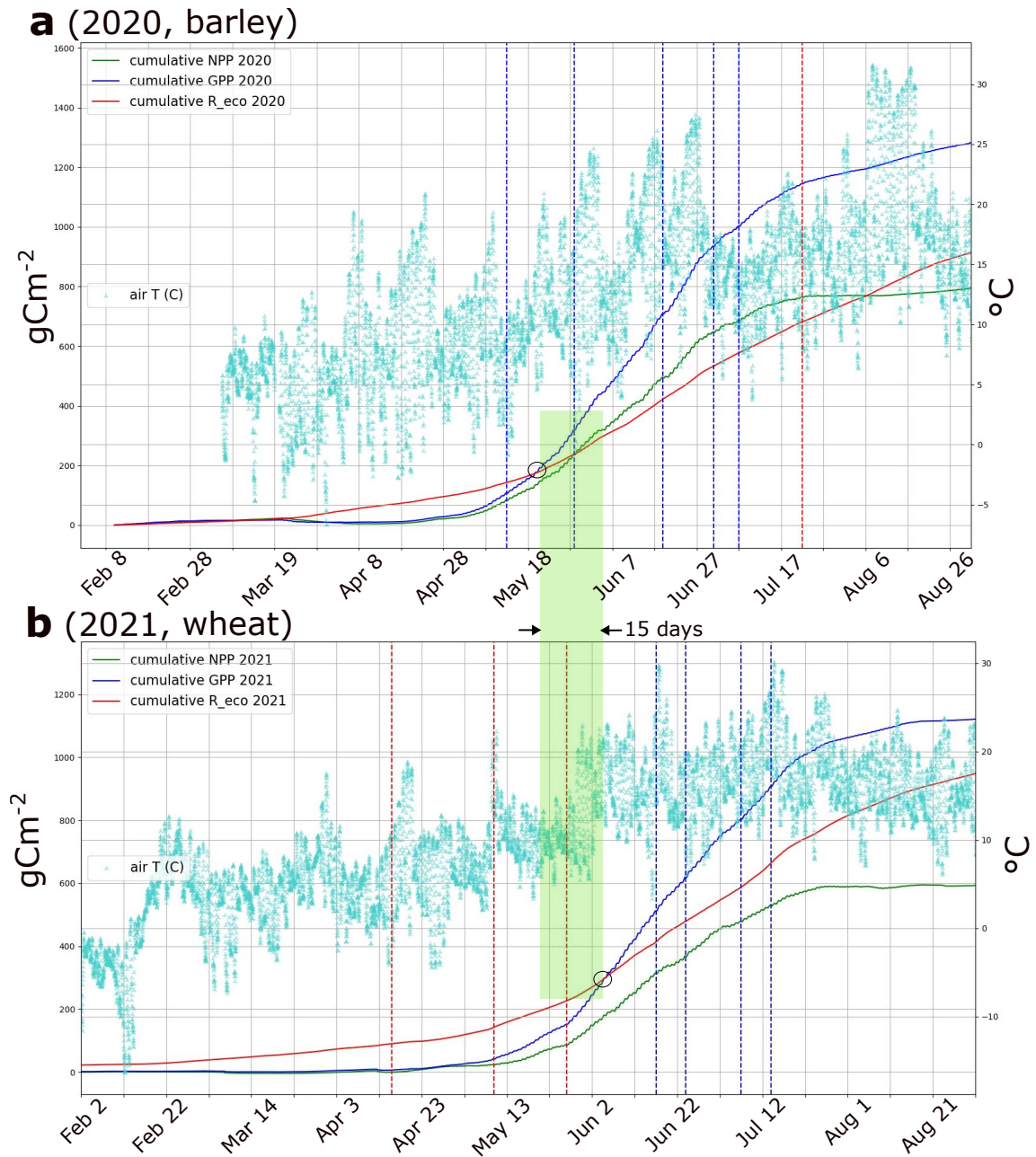online tool : www.bgc-jena.mpg.de/bgi/index.php/Services/REddyProcWeb.

Figure 12. Estimated cumulative fluxes along the growing season of 2020 (**a**), and 2021 (**b**). GPP: gross primary productivity; R_{eco}: ecosystem respiration; NPP: net primary productivity. The red vertical lines indicate aboveground biomass (AGB) sampling dates, while the blue lines indicate dates in which both AGB sampling and UAV-LiDAR surveys took place. In both years, the black circles indicate the dates when GPP offsets R_{eco}. It can be observed how in 2021 this occurs on the 5th June, while in 2020 GPP reaches ecosystem respiratory losses on the 19th May, i.e. 16 days earlier. This delay in GPP during 2021 is partly explained due to the cold spell of February, damaging the early seedlings. The lack of temperatures at the beginning of 2020 (**a**) is due to a failure in the instrumental setup.

References

[1]   David Laborde et al. "Agricultural subsidies and global greenhouse gas emissions". In: *Nature communications* 12.1 (2021), p. 2601.

[2]   John R Porter, Mark Howden, and Pete Smith. "Considering agriculture in IPCC assessments". In: *Nature Climate Change* 7.10 (2017), pp. 680–683.

[3]   Philip Thornton et al. "Agriculture in a changing climate: Keeping our cool in the face of the hothouse". In: *Outlook on Agriculture* 47.4 (2018), pp. 283–290.

[4]   P. R. Shukla et al. *Summary for policymakers, in Climate Change Land: An IPCC Special Report on Climate Change Desertification, Land Degradation, Sustainable Land Management, Food Security, Greenhouse Gas Fluxes in Terrestrial Ecosystems*. Tech. rep. Intergovernmental Panel on Climate Change, 2023.

[5]   Marco Springmann et al. "Options for keeping the food system within environmental limits". In: *Nature* 562.7728 (2018), pp. 519–525.

[6]   Gerald C Nelson et al. "Climate change effects on agriculture: Economic responses to biophysical shocks". In: *Proceedings of the National Academy of Sciences* 111.9 (2014), pp. 3274–3279.

[7]   Mitchell C Hunter et al. "Agriculture in 2050: recalibrating targets for sustainable intensification". In: *Bioscience* 67.4 (2017), pp. 386–391.

[8]   Hamid El Bilali et al. "Food and nutrition security and sustainability transitions in food systems". In: *Food and energy security* 8.2 (2019), e00154.

[9]   Jonathan A Foley et al. "Solutions for a cultivated planet". In: *Nature* 478.7369 (2011), pp. 337–342.

[10]   Tara Garnett et al. "Sustainable intensification in agriculture: premises and policies". In: *Science* 341.6141 (2013), pp. 33–34.

[11]   David J Mulla. "Twenty five years of remote sensing in precision agriculture: Key advances and remaining knowledge gaps". In: *Biosystems engineering* 114.4 (2013), pp. 358–371.

[12]   F Stuart Chapin, PA Matson, and PM Vitousek. *Principles of terrestrial ecosystem ecology. Principles of Terrestrial Ecosystem Ecology*. 2012.

[13]   YM Zhang et al. "Vegetation carbon sequestration in the Loess Plateau under the synergistic effects of land cover change and elevations". In: *Acta Ecologica Sinica* 42.10 (2022), pp. 3897–3908.

[14]   Peter M Anthoni et al. "Winter wheat carbon exchange in Thuringia, Germany". In: *Agricultural and Forest Meteorology* 121.1-2 (2004), pp. 55–67.

[15]   Ulises Mariano Marconato, Roberto J Fernández, and Gabriela Posse Beaulieu. *Cropland Net Ecosystem Exchange Estimation for the Inland Pampas (Argentina) Using EVI, Land Cover Maps, and Eddy Covariance Fluxes*. Tech. rep. Frontiers Media, 2022.

[16]   Arne Poyda et al. "Carbon fluxes and budgets of intensive crop rotations in two regional climates of southwest Germany". In: *Agriculture, Ecosystems & Environment* 276 (2019), pp. 31–46.

[17]   Anne-Katrin Prescher, Thomas Grünwald, and Christian Bernhofer. "Land use regulates carbon budgets in eastern Germany: From NEE to NBP". In: *Agricultural and Forest Meteorology* 150.7-8 (2010), pp. 1016–1025.

[18]   Rasmus Jensen, Mathias Herbst, and Thomas Friborg. *Direct and indirect controls of the interannual variability in atmospheric CO2 exchange of three contrasting ecosystems in Denmark.* 2016.

[19]   Praveena Krishnan et al. "Factors controlling the interannual variability in the carbon balance of a southern boreal black spruce forest". In: *Journal of Geophysical Research: Atmospheres* 113.D9 (2008).

[20]   Christopher B Field and Jörg Kaduk. "The carbon balance of an old-growth forest: building across approaches". In: *Ecosystems* 7 (2004), pp. 525–533.

[21]   Mark E Harmon et al. "Production, respiration, and overall carbon balance in an old-growth Pseudotsuga-Tsuga forest ecosystem". In: *Ecosystems* 7 (2004), pp. 498–512.

[22]   Heather Keith, Brendan G Mackey, and David B Lindenmayer. "Re-evaluation of forest biomass carbon stocks and lessons from the world's most carbon-dense forests". In: *Proceedings of the National Academy of Sciences* 106.28 (2009), pp. 11635–11640.

[23]   Scott D Miller et al. "Biometric and micrometeorological measurements of tropical forest carbon balance". In: *Ecological Applications* 14.sp4 (2004), pp. 114–126.

[24]   Jian Wu et al. "Synthesis on the carbon budget and cycling in a Danish, temperate deciduous forest". In: *Agricultural and Forest Meteorology* 181 (2013), pp. 94–107.

[25]   Thomas Foken, Marc Aubinet, and Ray Leuning. "The eddy covariance method". In: *Eddy covariance: a practical guide to measurement and data analysis.* Springer, 2011, pp. 1–19.

[26]   Sheng Wang et al. "Temporal interpolation of land surface fluxes derived from remote sensing–results with an unmanned aerial system". In: *Hydrology and Earth System Sciences* 24.7 (2020), pp. 3643–3661.

[27]   Helene Hoffmann et al. "Crop water stress maps for an entire growing season from visible and thermal UAV imagery". In: *Biogeosciences* 13.24 (2016), pp. 6545–6563.

[28]   Derek Hollenbeck and YangQuan Chen. "Multi-UAV method for continuous source rate estimation of fugitive gas emissions from a point source". In: *2021 International Conference on Unmanned Aircraft Systems (ICUAS)*. IEEE. 2021, pp. 1308–1313.

[29]   Derek Hollenbeck et al. "Evaluating a UAV-based mobile sensing system designed to quantify ecosystem-based methane". In: *Authorea Preprints* (2022).

[30]   Jaime C Revenga et al. "Above-Ground Biomass Prediction for Croplands at a Sub-Meter Resolution Using UAV–LiDAR and Machine Learning Methods". In: *Remote Sensing* 14.16 (2022), p. 3912.

[31]   N Ace Pugh et al. "Temporal estimates of crop growth in sorghum and maize breeding enabled by unmanned aerial systems". In: *The Plant Phenome Journal* 1.1 (2018), pp. 1–10.

[32]   Wang Li et al. "Remote estimation of canopy height and aboveground biomass of maize using high-resolution stereo images from a low-cost unmanned aerial vehicle system". In: *Ecological indicators* 67 (2016), pp. 637–648.

[33]   Abdullah M Al-Sadi et al. "Genetic analysis reveals diversity and genetic relationship among Trichoderma isolates from potting media, cultivated soil and uncultivated soil". In: *BMC microbiology* 15 (2015), pp. 1–11.

[34]   Sebastian Varela et al. "Spatio-temporal evaluation of plant height in corn via unmanned aerial systems". In: *Journal of Applied Remote Sensing* 11.3 (2017), pp. 036013–036013.

[35]   J Bendig et al. "Very high resolution crop surface models (CSMs) from UAV-based stereo images for rice growth monitoring in Northeast China". In: *Int. Arch. Photogramm. Remote Sens. Spat. Inf. Sci* 40 (2013), pp. 45–50.

[36]   Juliane Bendig et al. "Estimating biomass of barley using crop surface models (CSMs) derived from UAV-based RGB imaging". In: *Remote sensing* 6.11 (2014), pp. 10395–10412.

[37]   Sebastian Brocks and Georg Bareth. "Estimating barley biomass with crop surface models from oblique RGB imagery". In: *Remote Sensing* 10.2 (2018), p. 268.

[38]   Tianxing Chu et al. "Cotton growth modeling and assessment using unmanned aircraft system visual-band imagery". In: *Journal of Applied Remote Sensing* 10.3 (2016), pp. 036018–036018.

[39]   T Jensen et al. "Detecting the attributes of a wheat crop using digital imagery acquired from a low-altitude platform". In: *Computers and electronics in agriculture* 59.1-2 (2007), pp. 66–77.

[40]   E Raymond Hunt et al. "NIR-green-blue high-resolution digital images for assessment of winter cover crop biomass". In: *GIScience & remote sensing* 48.1 (2011), pp. 86–98.

[41]   Maria Tattaris, Matthew P Reynolds, and Scott C Chapman. "A direct comparison of remote sensing approaches for high-throughput phenotyping in plant breeding". In: *Frontiers in plant science* 7 (2016), p. 1131.

[42]   Jakob Geipel et al. "A programmable aerial multispectral camera system for in-season crop biomass and nitrogen content estimation". In: *Agriculture* 6.1 (2016), p. 4.

[43]   Jibo Yue et al. "Estimation of winter wheat above-ground biomass using unmanned aerial vehicle-based snapshot hyperspectral sensor and crop height improved models". In: *Remote Sensing* 9.7 (2017), p. 708.

[44]   Roope Näsi et al. "Estimating biomass and nitrogen amount of barley and grass using UAV and aircraft based spectral and photogrammetric 3D features". In: *Remote Sensing* 10.7 (2018), p. 1082.

[45]   Angela Kross et al. "Assessment of RapidEye vegetation indices for estimation of leaf area index and biomass in corn and soybean crops". In: *International Journal of Applied Earth Observation and Geoinformation* 34 (2015), pp. 235–248.

[46]   Kishore C Swain, Steven J Thomson, and Hemantha PW Jayasuriya. "Adoption of an unmanned helicopter for low-altitude remote sensing to estimate yield and total biomass of a rice crop". In: *Transactions of the ASABE* 53.1 (2010), pp. 21–27.

[47]   Jordan Steven Bates et al. "Estimating canopy density parameters time-series for winter wheat using UAS Mounted LiDAR". In: *Remote Sensing* 13.4 (2021), p. 710.

[48]   ICOS. *Integrated Carbon Observation System*. 2023. URL: https://www.icos-cp.eu/ (visited on 02/04/2023).

[49]   Danish Ministry of Environment. *Order on the use of fertilisers by agriculture for the 2020/2021 planning period*. 2021. URL: https://www.retsinformation.dk/eli/lta/2020/1166. (accessed: 25.10.2021).

[50]   L Davidson et al. "Airborne to UAS LiDAR: An analysis of UAS LiDAR ground control targets". In: *ISPRS Geospatial Week 2019* (2019).

[51]   Bert Gielen et al. "Ancillary vegetation measurements at ICOS ecosystem stations". In: *International Agrophysics* 32.4 (2018), pp. 645–664.

[52] Teng Hu et al. "Root biomass in cereals, catch crops and weeds can be reliably estimated without considering aboveground biomass". In: *Agriculture, Ecosystems & Environment* 251 (2018), pp. 141–148.

[53] Yakov Kuzyakov and Grzegorz Domanski. "Carbon input by plants into the soil. Review". In: *Journal of Plant Nutrition and Soil Science* 163.4 (2000), pp. 421–431.

[54] JA Palta and PJ Gregory. "Drought affects the fluxes of carbon to roots and soil in 13C pulse-labelled plants of wheat". In: *Soil Biology and Biochemistry* 29.9-10 (1997), pp. 1395–1403.

[55] Jan C Zadoks, Ting T Chang, Cal F Konzak, et al. "A decimal code for the growth stages of cereals." In: *Weed research* 14.6 (1974), pp. 415–421.

[56] Erick Zagal, Sigfus Bjarnason, and ULF Olsson. "Carbon and nitrogen in the root-zone of barley (Hordeum vulgare L.) supplied with nitrogen fertilizer at two rates". In: *Plant and Soil* 157 (1993), pp. 51–63.

[57] S Sabbatini and D Papale. *ICOS Ecosystem Instructions for Turbulent Flux Measurements of CO2, Energy and Momentum (Version 20180110), ICOS Ecosystem Thematic Centre.* 2017.

[58] Dean Vickers and L Mahrt. "Quality control and flux sampling problems for tower and aircraft data". In: *Journal of atmospheric and oceanic technology* 14.3 (1997), pp. 512–526.

[59] E. K. Webb, G. I. Pearman, and R. Leuning. "Correction of flux measurements for density effects due to heat and water vapour transfer". In: *Quarterly Journal of the Royal Meteorological Society* 106.447 (1980), pp. 85–100.

[60] Claudia Liebethal and Thomas Foken. "On the significance of the Webb correction to fluxes". In: *Boundary-Layer Meteorology* 109 (2003), pp. 99–106.

[61] JB Moncrieff et al. "A system to measure surface fluxes of momentum, sensible heat, water vapour and carbon dioxide". In: *Journal of Hydrology* 188 (1997), pp. 589–611.

[62] Dario Papale et al. "Towards a standardized processing of Net Ecosystem Exchange measured with eddy covariance technique: algorithms and uncertainty estimation". In: *Biogeosciences* 3.4 (2006), pp. 571–583.

[63] Markus Reichstein et al. "On the separation of net ecosystem exchange into assimilation and ecosystem respiration: review and improved algorithm". In: *Global change biology* 11.9 (2005), pp. 1424–1439.

[64] Natascha Kljun, MW Rotach, and HP Schmid. "A three-dimensional backward Lagrangian footprint model for a wide range of boundary-layer stratifications". In: *Boundary-Layer Meteorology* 103 (2002), pp. 205–226.

[65] Scott Goetz and Ralph Dubayah. "Advances in remote sensing technology and implications for measuring and monitoring forest carbon stocks and change". In: *Carbon Management* 2.3 (2011), pp. 231–244.

[66] Francis Stuart Chapin et al. "Principles of terrestrial ecosystem ecology". In: (2002).

[67] John Lloyd and JA Taylor. "On the temperature dependence of soil respiration". In: *Functional ecology* (1994), pp. 315–323.

[68] Peter J Huber. "Robust statistics". In: *International encyclopedia of statistical science.* Springer, 2011, pp. 1248–1251.

[69] Art B Owen. "A robust hybrid of lasso and ridge regression". In: *Contemporary Mathematics* 443.7 (2007), pp. 59–72.

[70]   Pierre Geurts, Damien Ernst, and Louis Wehenkel. "Extremely randomized trees". In: *Machine learning* 63.1 (2006), pp. 3–42.

[71]   Tianqi Chen et al. "Xgboost: extreme gradient boosting". In: *R package version 0.4-2* 1.4 (2015), pp. 1–4.

[72]   Leo Breiman. "Random forests". In: *Machine learning* 45.1 (2001), pp. 5–32.

[73]   Ernest C Large et al. "Growth stages in cereals. Illustration of the Feekes scale." In: *Plant pathology* 3 (1954), pp. 128–129.

[74]   Iker Aranjuelo et al. "Carbon and nitrogen partitioning during the post-anthesis period is conditioned by N fertilisation and sink strength in three cereals". In: *Plant Biology* 15.1 (2013), pp. 135–143.

[75]   Joaquin Quinonero-Candela et al. *Dataset shift in machine learning.* Mit Press, 2008.

[76]   Shai Ben-David et al. "A theory of learning from different domains". In: *Machine learning* 79 (2010), pp. 151–175.

[77]   Liisa Pietola and Laura Alakukku. "Root growth dynamics and biomass input by Nordic annual field crops". In: *Agriculture, ecosystems & environment* 108.2 (2005), pp. 135–144.

[78]   MA Bolinder, DA Angers, and JP Dubuc. "Estimating shoot to root ratios and annual carbon inputs in soils for cereal crops". In: *Agriculture, ecosystems & environment* 63.1 (1997), pp. 61–66.

[79]   Judah D Grossman and Kevin J Rice. "Evolution of root plasticity responses to variation in soil nutrient distribution and concentration". In: *Evolutionary Applications* 5.8 (2012), pp. 850–857.

[80]   Assaf Distelfeld, Raz Avni, and Andreas M Fischer. "Senescence, nutrient remobilization, and yield in wheat and barley". In: *Journal of experimental botany* 65.14 (2014), pp. 3783–3798.

[81]   Per L Gregersen. "Senescence and nutrient remobilization in crop plants". In: *The molecular and physiological basis of nutrient use efficiency in crops* (2011), pp. 83–102.

[82]   Ngonidzashe Chirinda, Jørgen E Olesen, and John R Porter. "Root carbon input in organic and inorganic fertilizer-based systems". In: *Plant and Soil* 359 (2012), pp. 321–333.

[83]   Afshin Soltani. *Modeling physiology of crop development, growth and yield.* CABi, 2012.